

Casimir forces in the time domain: Applications

Alexander P. McCauley,¹ Alejandro W. Rodriguez,¹ John D. Joannopoulos,¹ and Steven G. Johnson²

¹*Department of Physics, Massachusetts Institute of Technology, Cambridge, MA 02139*

²*Department of Mathematics, Massachusetts Institute of Technology, Cambridge, MA 02139*

Our preceding paper, Ref. 1, introduced a method to compute Casimir forces in arbitrary geometries and for arbitrary materials that was based on a finite-difference time-domain (FDTD) scheme. In this manuscript, we focus on the efficient implementation of our method for geometries of practical interest and extend our previous proof-of-concept algorithm in one dimension to problems in two and three dimensions, introducing a number of new optimizations. We consider Casimir piston-like problems with nonmonotonic and monotonic force dependence on sidewall separation, both for previously solved geometries to validate our method and also for new geometries involving magnetic sidewalls and/or cylindrical pistons. We include realistic dielectric materials to calculate the force between suspended silicon waveguides or on a suspended membrane with periodic grooves, also demonstrating the application of PML absorbing boundaries and/or periodic boundaries. In addition we apply this method to a realizable three-dimensional system in which a silica sphere is stably suspended in a fluid above an indented metallic substrate. More generally, the method allows off-the-shelf FDTD software, already supporting a wide variety of materials (including dielectric, magnetic, and even anisotropic materials) and boundary conditions, to be exploited for the Casimir problem.

I. INTRODUCTION

The Casimir force, arising due to quantum fluctuations of the electromagnetic field [2], has been widely studied over the past few decades [3, 4, 5, 6] and verified by many experiments. Until recently, most works on the subject had been restricted to simple geometries, such as parallel plates or similar approximations thereof. However, new theoretical methods capable of computing the force in arbitrary geometries have already begun to explore the strong geometry dependence of the force and have demonstrated a number of interesting effects [7, 8, 9, 10, 11, 12, 13, 14, 15, 16]. A substantial motivation for the study of this effect is due to recent progress in the field of nano-electro-mechanical systems (MEMS), where Casimir forces have been observed [17] and may play a significant role in “stiction” and other phenomena involving small surface separations. Currently, most work on Casimir forces is carried out by specialists in the field. In order to help open this field to other scientists and engineers, such as the MEMS community, we believe it fruitful to frame the calculation of the force in a fashion that may be more accessible to broader audiences.

In Ref. 1, with that goal in mind, we introduced a theoretical framework for computing Casimir forces via the standard finite-difference time-domain (FDTD) method of classical computational electromagnetism [18] (for which software is already widely available). The purpose of this manuscript is to describe how these computations may be implemented in higher dimensions and to demonstrate the flexibility and strengths of this approach. In particular, we demonstrate calculations of Casimir forces in two- and three-dimensional geometries, including three-dimensional geometries without any rotational or translational symmetry. Furthermore, we de-

scribe a harmonic expansion technique that substantially increases the speed of the computation for many systems, allowing Casimir forces to be efficiently computed even on single computers, although parallel FDTD software is also common and greatly expands the range of accessible problems.

Our manuscript is organized as follows: First, in Sec. II, we briefly describe the algorithm presented in Ref. 1 to compute Casimir forces in the time domain. This is followed by an important modification involving a harmonic expansion technique that greatly reduces the computational cost of the method. Second, Sec. III presents a number of calculations in two- and three-dimensional geometries. In particular, Sec. III A presents calculations of the force in the piston-like structure of Ref. 8, and these are checked against previous results. These calculations demonstrate both the validity of our approach and the desirable properties of the harmonic expansion. In subsequent sections, we demonstrate computations exploiting various symmetries in three dimensions: translation-invariance, cylindrical symmetry, and periodic boundaries. These symmetries transform the calculation into the solution of a set of two-dimensional problems. Finally in Sec. III E we demonstrate a fully three-dimensional computation involving the stable levitation of a sphere in a high-dielectric fluid above an indented metal surface. We exploit a freely available FDTD code [19], which handles symmetries and cylindrical coordinates and also is scriptable/programmable in order to automatically run the sequence of FDTD simulations required to determine the Casimir force [20]. Finally, in the Appendix, we present details of the derivations of the harmonic expansion and an optimization of the computation of $g(t)$.

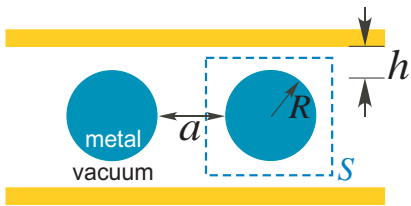


FIG. 1: Schematic showing the two-dimensional piston-like configuration of [22]: Two perfectly conducting circular cylinders of radius R , separated by a distance a , are sandwiched between two perfectly conducting plates (the materials are either perfect metallic or perfect magnetic conductors). The separation between the blocks and the cylinder surface is denoted as h .

II. HARMONIC EXPANSION

In this section we briefly summarize the method of Ref. 1, and introduce an additional step which greatly reduces the computational cost of running simulations in higher dimensions.

In Ref. 1, we described a method to calculate Casimir forces in the time domain. Our approach involves a modification of the well-known stress-tensor method [21], in which the force on an object can be found by integrating the Minkowski stress tensor around a surface S surrounding the object (Fig. 1), and over all frequencies. Our recent approach [1] abandons the frequency domain altogether in favor of a purely time-domain scheme in which the force on an object is computed via a series of independent FDTD calculations in which sources are placed at each point on S . The electromagnetic response to these sources is then integrated in time against a pre-determined function $g(-t)$.

The main purpose of this approach is to compute the effect of the entire frequency spectrum in a single simulation for each source, rather than a separate set of calculations for each frequency as in most previous work [12].

We exactly transform the problem into a mathematically equivalent system in which an arbitrary dissipation is introduced. This dissipation will cause the electromagnetic response to converge rapidly, greatly reducing the simulation time. In particular, a frequency-independent, spatially uniform conductivity σ is chosen so that the force will converge very rapidly as a function of simulation time. For all values of σ , the force will converge to the same value, but the optimal σ results in the shortest simulation time and will depend on the system under consideration. Unless otherwise stated, for the simulations in this paper, we use $\sigma = 1$ (in units of $2\pi c/a$, a being a typical length scale in the problem).

In particular, the Casimir force is given by:

$$F_i = \text{Im} \frac{\hbar}{\pi} \int_0^\infty dt g(-t) (\Gamma_i^E(t) + \Gamma_i^H(t)), \quad (1)$$

where $g(t)$ is a geometry-independent function discussed further in the Appendix, and the $\Gamma(t)$ are functions of

the electromagnetic fields on the surface S defined in our previous work [1].

Written in terms of the electric field response in direction i at (t, \mathbf{x}) to a source current $J(t, \mathbf{x}) = \delta(t)\delta(\mathbf{x} - \mathbf{x}')$ in direction j , $E_{ij}(t; \mathbf{x}, \mathbf{x}')$, the quantity $\Gamma_i^E(t)$ is defined as:

$$\begin{aligned} \Gamma_i^E(t) &\equiv \int_S dS_j(\mathbf{x}) \left(E_{ij}(t; \mathbf{x}, \mathbf{x}) - \frac{1}{2} \delta_{ij} \sum_k E_{kk}(t; \mathbf{x}, \mathbf{x}) \right) \\ &\equiv \int dS_j(\mathbf{x}) \Gamma_{ij}^E(t; \mathbf{x}, \mathbf{x}) \end{aligned}$$

where $dS_j(\mathbf{x}) \equiv dS(\mathbf{x}) n_j(\mathbf{x})$, $dS(\mathbf{x})$ the differential area element and $\mathbf{n}(\mathbf{x})$ is the unit normal vector to S at \mathbf{x} . A similar definition holds for $\Gamma_i^H(t)$ involving the magnetic field Green's function H_{ij} .

As described in Ref. 1, computation of the Casimir force entails finding both $\Gamma^E(t; \mathbf{x}, \mathbf{x})$ and the $\Gamma^H(t; \mathbf{x}, \mathbf{x})$ field response with a separate time-domain simulation for every point $\mathbf{x} \in S$.

While each individual simulation can be performed very efficiently on modern computers, the surface S will, in general, consist of hundreds or thousands of pixels or voxels. This requires a large number of time-domain simulations, this number being highly dependent upon the resolution and shape of S , making the computation potentially very costly in practice.

We can dramatically reduce the number of required simulations by reformulating the force in terms of a harmonic expansion in $\Gamma^E(t; \mathbf{x}, \mathbf{x})$, involving the distributed field responses to distributed currents. This is done as follows [an analogous derivation holds for $\Gamma^H(t; \mathbf{x}, \mathbf{x})$]:

As S is assumed to be a compact surface, we can rewrite $\Gamma_{ij}(t; \mathbf{x}, \mathbf{x})$ as an integral over S :

$$\Gamma_{ij}^E(t; \mathbf{x}, \mathbf{x}) = \int_S dS(\mathbf{x}') \Gamma_{ij}^E(t; \mathbf{x}, \mathbf{x}') \delta_S(\mathbf{x} - \mathbf{x}') \quad (2)$$

where in this integral dS is a scalar unit of area, and δ_S denotes a δ -function with respect to integrals over the surface S . Given a set of orthonormal basis functions $\{f_n(\mathbf{x})\}$ defined on and complete over S , we can make the following expansion of the δ function, valid for all points $\mathbf{x}, \mathbf{x}' \in S$:

$$\delta_S(\mathbf{x} - \mathbf{x}') = \sum_n \bar{f}_n(\mathbf{x}) f_n(\mathbf{x}') \quad (3)$$

The $f_n(\mathbf{x})$ can be an arbitrary set of functions, assuming that they are complete and orthonormal on S [31].

Inserting this expansion of the δ -function into Equation (2) and rearranging terms yields:

$$\Gamma_{ij}^E(t; \mathbf{x}, \mathbf{x}) = \sum_n \bar{f}_n(\mathbf{x}) \left(\int_S dS(\mathbf{x}') \Gamma_{ij}^E(t; \mathbf{x}, \mathbf{x}') f_n(\mathbf{x}') \right) \quad (4)$$

The term in parentheses can be understood in a physical context: it is the electric-field response at position \mathbf{x} and

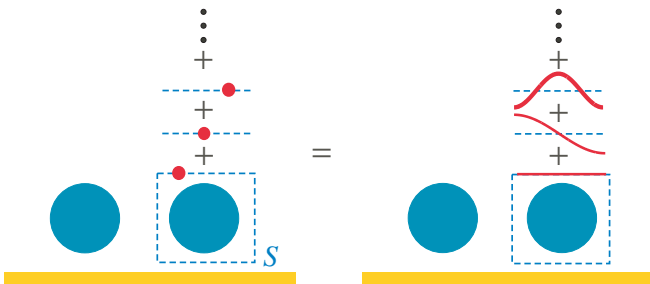


FIG. 2: Differing harmonic expansions of the source currents (red) on the surface S . The left part shows an expansion using point sources, where each dot represents a different simulation. The right part corresponds to using $f_n(\mathbf{x}) \sim \cos(x)$ for each side of S . Either basis forms a complete basis for all functions in S .

time t to a current source on the surface S of the form $J(\mathbf{x}, t) = \delta(t)f_n(\mathbf{x})$. We denote this quantity by $\Gamma_{ij;n}^E$:

$$\Gamma_{ij;n}^E(t, \mathbf{x}) \equiv \int_S dS(\mathbf{x}') \Gamma_{ij}^E(t; \mathbf{x}, \mathbf{x}') f_n(\mathbf{x}') \quad (5)$$

where the n subscript indicates that this is a field in response to a current source determined by $f_n(\mathbf{x})$. $\Gamma_{ij;n}^E(t, \mathbf{x})$ is exactly what can be measured in an FDTD simulation using a current $J(\mathbf{x}, t) = \delta(t)f_n(\mathbf{x})$ for each n . This equivalence is illustrated in Fig. 2.

The procedure is now only slightly modified from the one outlined in Ref. 1: after defining a geometry and a surface S of integration, one will additionally need to specify a set of harmonic basis functions $\{f_n(x)\}$ on S . For each harmonic moment n , one inserts a current function $\mathbf{J}(\mathbf{x}, t) = \delta(t)f_n(\mathbf{x})$ on S and measures the field response $\Gamma_{ij;n}(\mathbf{x}, t)$. Summing over all harmonic moments will yield the total force.

In the following section, we take as our harmonic source basis the Fourier cosine series for each side of S considered separately, which provides a convenient and efficient basis for computation. We then illustrate its application to systems of perfect conductors and dielectrics in two and three dimensions. Three-dimensional systems with cylindrical symmetry are treated separately, as the harmonic expansion (as derived in the Appendix) becomes considerably simpler in this case.

III. NUMERICAL IMPLEMENTATION

In principle, any surface S and any harmonic source basis can be used. Point sources, as discussed in Ref. 1, are a simple, although highly inefficient, example. However, many common FDTD algorithms (including the one we employ in this paper) involve simulation on a discretized grid. For these applications, a rectangular surface S with an expansion basis separately defined on each face of S is the simplest. In this case, the field integration along each face can be performed to high accuracy and

converges rapidly. The Fourier cosine series on a discrete grid is essentially a discrete cosine transform (DCT), a well known discrete orthogonal basis with rapid convergence properties [23]. This in contrast to discretizing some basis such as spherical harmonics that are only approximately orthogonal when discretized on a rectangular grid.

A. Two-dimensional systems

In this section we consider a variant of the piston-like configuration of Ref. 8, shown as the inset to Fig. 3. This system consists of two cylindrical rods sandwiched between two sidewalls, and is of interest due to the non monotonic dependence of the Casimir force between the two blocks as the vertical wall separation h/a is varied. The case of perfect metallic sidewalls ($\varepsilon(x) = -\infty$) has been solved previously [22]; here we also treat the case of perfect magnetic conductor sidewalls ($\mu(x) = -\infty$) as a simple demonstration of method using magnetic materials.

While three-dimensional in nature, the system is translation-invariant in the z -direction and involves only perfect metallic or magnetic conductors. As discussed in Ref. 12 this situation can actually be treated as the two-dimensional problem depicted in Fig. 2 using a slightly different form for $g(-t)$ in Eq. (1) (given in the Appendix). The reason we consider the three-dimensional case is that we can directly compare the results for the case of metallic sidewalls to the high-precision scattering calculations of Ref. 22 (which uses a specialized exponentially convergent basis for cylinder/plane geometries).

For this system, the surface S consists of four faces, each of which is a line segment of some length L parametrized by a single variable x . We employ a cosine basis for our harmonic expansion on each face of S . The basis functions for each side are then:

$$f_n(x) = \sqrt{\frac{2}{L}} \cos\left(\frac{n\pi x}{L}\right), \quad n = 0, 1, \dots \quad (6)$$

where L is the length of the edge, and $f_n(x) = 0$ for all points x not on that edge of S . These functions, and their equivalence to a computation using δ -function sources as basis functions, are shown in Fig. 2.

In the case of our FDTD algorithm, space is discretized on a Yee grid [18], and in most cases x will turn out to lie in between two grid points. One can run separate simulations in which each edge of S is displaced in the appropriate direction so that all of its sources lie on a grid point. However, we find that it is sufficient to place suitably averaged currents on neighboring grid points, as several available FDTD implementations provide features to accurately interpolate currents from any location onto the grid.

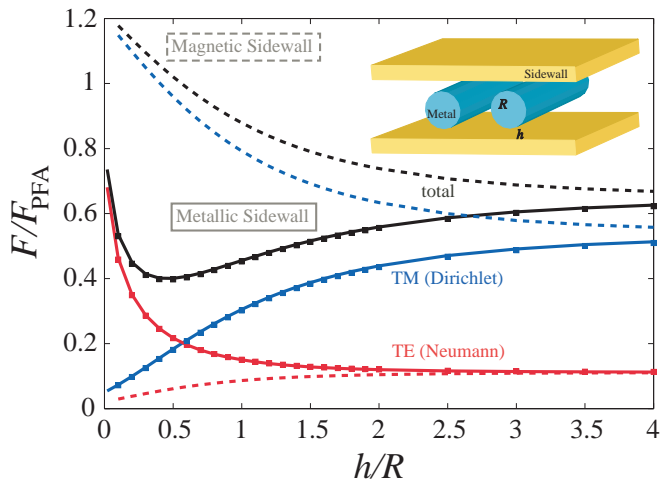


FIG. 3: Force for the double cylinders of [22] as a function of sidewall separation h/a , normalized by the PFA force $F_{\text{PFA}} = \hbar c \zeta(3) d / 8\pi a^3$. Red/blue/black squares show the TE/TM/total force in the presence of metallic sidewalls, as computed by the FDTD method (squares). The solid lines indicate the results from the scattering calculations of [22], showing excellent agreement. Dashed lines indicate the same force components, but in the presence of perfect magnetic-conductor sidewalls (computed via FDTD). Note that the total force is nonmonotonic for electric sidewalls and monotonic for magnetic sidewalls.

The force, as a function of the vertical sidewall separation h/a , and for both TE and TM field components, is shown in Fig. 3 and checked against previously known results for the case of perfect metallic sidewalls [22]. We also show the force (dashed lines) for the case of perfect magnetic conductor sidewalls.

In the case of metallic sidewalls, the force is nonmonotonic in h/a . As explained in Ref. 22, this is due to the competition between the TM force, which dominates for large h/a but is suppressed for small h/a , and the TE force, which has the opposite behavior, explained via the method of images for the conducting walls. Switching to perfect magnetic conductor sidewalls causes the TM force to be enhanced for small h/a and the TE force to be suppressed, because the image currents flip sign for magnetic conductors compared to electric conductors. As shown in Fig. 3, this results in a monotonic force for this case.

The result of the above calculation is a time-dependent field similar to that of Fig. 4, which when manipulated as prescribed in the previous section, will yield the Casimir force. As in Ref. 1, our ability to express the force for a dissipationless system (perfect-metal blocks in vacuum) in terms of the response of an artificial dissipative system ($\sigma \neq 0$) means that the fields, such as those shown in Fig. 4, rapidly decay away, and hence only a short simulation is required for each source term.

In addition, Fig. 5 shows the convergence of the harmonic expansion as a function of n . Asymptotically for

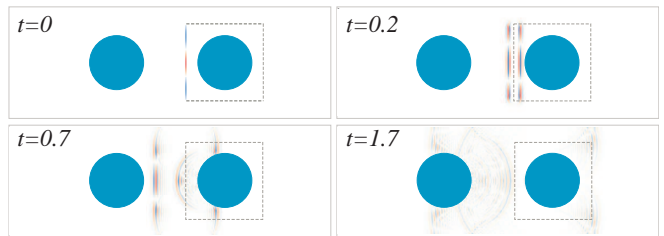


FIG. 4: $\Gamma_{yy;n=2}^E(t, \mathbf{x})$ snapshots (blue/white/red = positive/zero/negative) for the $n = 2$ term in the harmonic cosine expansion on the leftmost face of S for the double blocks configuration of [8] at selected times (in units of a/c).

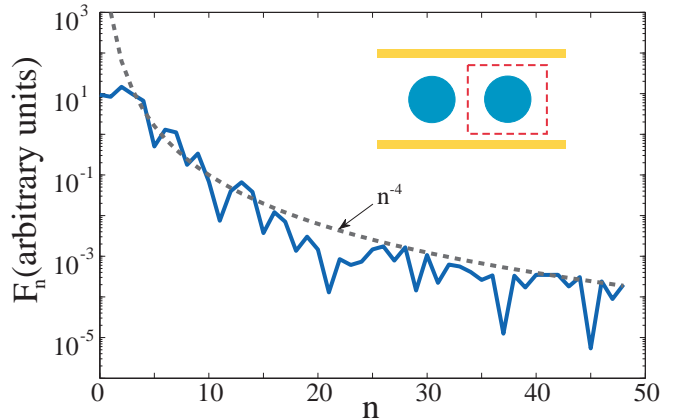


FIG. 5: Relative contribution of harmonic moment n in the cosine basis to the total Casimir force for the double blocks configuration (shown in the inset)

large n , an $n^{-1/4}$ power law is clearly discernible. The explanation for this convergence follows readily from the geometry of S : the electric field $\mathbf{E}(\mathbf{x})$, when viewed as a function along S , will have nonzero first derivatives at the corners. However, the cosine series used here always has a vanishing derivative. This implies that its cosine transform components will decay asymptotically as n^{-2} [24]. As Γ^E is related to the correlation function $\langle \mathbf{E}(\mathbf{x})\mathbf{E}(\mathbf{x}) \rangle$, their contributions will decay as n^{-4} . One could instead consider a Fourier series defined around the whole perimeter of S , but the convergence rate will be the same because the derivatives of the fields will be discontinuous around the corners of S . A circular surface would have no corners in the continuous case, but on a discretized grid would effectively have many corners and hence poor convergence with resolution.

B. Dispersive Materials

Dispersion in FDTD in general requires fitting an actual dispersion to a simple model (eg. a series of Lorentzians or Drude peaks). Assuming this has been done, these models can then be analytically continued onto the complex conductivity contour.

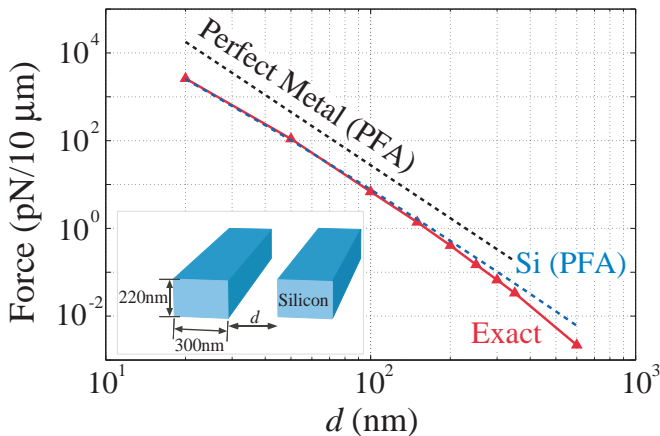


FIG. 6: Force per unit length between long silicon waveguides suspended in air [25], determined by the FDTD method (red triangles). Also shown is the analogous one-dimensional computation assuming silicon plates of finite thickness (blue dashes), and the result $F = \pi^2/240d^4A$ for perfect metals (assuming plate area A equal to the interaction area of the waveguides).

As an example of a calculation involving dispersive materials, we consider in this section a geometry recently used to measure the classical optical force between two suspended waveguides [25], confirming a prediction [26] that the sign of the classical force depends on the relative phase of modes excited in the two waveguides. We now compute the Casimir force in the same geometry, which consists of two identical silicon waveguides in empty space. We model silicon as a dielectric with dispersion given by:

$$\varepsilon(\omega) = \varepsilon_f + \frac{\varepsilon_f - \varepsilon_0}{1 - \left(\frac{\omega}{\omega_0}\right)^2} \quad (7)$$

where $\omega_0 = 6.6 \times 10^{15}$ rad/sec, and $\varepsilon_0 = 1.035$, $\varepsilon_f = 11.87$. This dispersion can be implemented in FDTD by the standard technique of auxiliary differential equations [18] mapped into the complex- ω plane as explained in Ref. 1.

The system is translation-invariant in the z direction. If it consisted only of perfect conductors, we could use the trick of the previous section and compute the force in only one 2d simulation. However, dielectrics hybridize the two polarizations and require an explicit k_z integral, as discussed in Ref. 12. Each value of k_z corresponds to a separate two-dimensional simulation with Bloch-periodic boundary conditions. The value of the force for each k_z is smooth and rapidly decaying, so in general only a few k_z points are needed.

To simulate the infinite open space around the waveguides, it is ideal to have “absorbing boundaries” so that waves from sources on S do not reflect back from the boundaries. We employ the standard technique of perfectly matched layers (PML), which are a thin layer of artificial absorbing material placed adjacent to the bound-

ary and designed to have nearly zero reflections [18]. The results are shown in red in Fig. 6. We also show (in blue) the force obtained using the proximity force approximation (PFA) calculations based on the Lifshitz formula [27, 28]. For the PFA, we assume two parallel silicon plates, infinite in both directions perpendicular to the force and having the same thickness as the waveguides in the direction parallel to the force, computing the PFA contribution from the surface area of the waveguide. As expected, at distances smaller than the waveguide width, the actual and PFA results are in good agreement, while as the waveguide separation increases, the PFA becomes more inaccurate. For example, by a separation of 300nm, the PFA result is off by 50%. We also show for comparison the force for the same surface between two perfectly metallic plates, also assuming infinite extent in both transverse directions.

C. Three dimensions with cylindrical symmetry

In the case of cylindrical symmetry, we can employ a cylindrical surface S and a complex exponential basis $e^{im\phi}$ in the ϕ direction. For a geometry with cylindrical symmetry and a separable source with $e^{im\phi}$ dependence, the resulting fields are also separable with the same ϕ dependence, and the unknowns reduce to a two-dimensional (r, z) problem for each m . This results in a substantial reduction in computational costs compared to a full three-dimensional computation.

Treating the reduced system as a two-dimensional space with coordinates (r, z) , the expression for the force (as derived in the Appendix) is now:

$$F_i = \sum_n \int_0^\infty dt \operatorname{Im}[g(-t)] \int_S ds_j(\mathbf{x}) \Gamma_{ij;n}(\mathbf{x}, t) \quad (8)$$

where the m -dependence has been absorbed into the definition of Γ above:

$$\Gamma_{ij;n}(x, t) \equiv \Gamma_{ij;n,m=0}(\mathbf{x}, t) + 2 \sum_{m>0} \operatorname{Re}[\Gamma_{ij;n,m}(\mathbf{x}, t)], \quad (9)$$

and $ds_j = ds n_j(\mathbf{x})$, ds being a one-dimensional Cartesian line element. As derived in the Appendix, the Jacobian factor r obtained from converting to cylindrical coordinates cancels out, so that the one-dimensional (r -independent) measure ds is the appropriate one to use in the surface integration. Also, the $2 \operatorname{Re}[\dots]$ comes from the fact that the $+m$ and $-m$ terms are complex conjugates. Although the exponentials $e^{im\phi}$ are complex, only the real part of the field response appears in Eq. (9), allowing us to use $\operatorname{Im}[g(-t)]$ alone in Eq. (8).

Given an $e^{im\phi}$ dependence in the fields, one can write Maxwell’s equations in cylindrical coordinates to obtain a two-dimensional equation involving only the fields in the (r, z) plane. This simplification is incorporated into many FDTD solvers, as in the one we currently employ [19], with the computational cell being restricted to the (r, z)

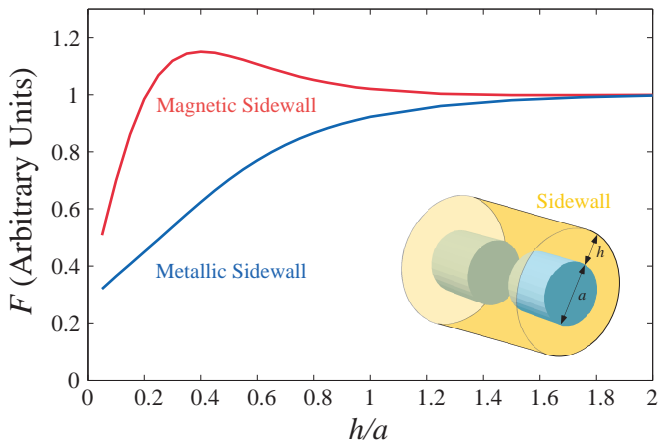


FIG. 7: Force as a function of outer sidewall spacing h/a for the cylindrically-symmetric piston configuration shown in the figure. Both plates are perfect metals, and the forces for both perfect metallic and perfect magnetic conductor sidewalls are shown. Note that in contrast to Fig. 3, here the force is monotonic in h/a for the metallic case and non monotonic for the magnetic case.

plane and m appearing as a parameter. When this is the case, the implementation of cylindrical symmetry is almost identical to the two-dimensional situation. The only difference is that now there is an additional index m over which the force must be summed.

To illustrate the use of this algorithm with cylindrical symmetry, we examine the 3d system shown in the inset of Fig. 7. This configuration is similar to the configuration of cylindrical rods of Fig. 3, except that instead of translational (z) invariance we instead impose rotational (ϕ) invariance. In this case, the two sidewalls are joined to form a cylindrical tube. We examine the force between the two blocks as a function of h/a (the $h = 0$ case has been solved analytically [29]).

Due to the two-dimensional nature of this problem, computation time is comparable to that of the two-dimensional double block geometry of the previous section. Rough results (at resolution 40, accurate to within a few percentage points) can be obtained rapidly on a single computer (about 5 minutes running on 8 processors) are shown in Fig. 7 for each value of h/a . Only indices $n, m \in \{0, 1, 2\}$ are needed for the result to have converged to within 1%, after which the error is dominated by the spatial discretization. PML is used along the top and bottom walls of the tube.

In contrast to the case of two pistons with translational symmetry, the force for metallic sidewalls is monotonic in h/a . Somewhat surprisingly, when the sidewalls are switched to perfect magnetic conductors the force becomes non monotonic again. Although the use of perfectly magnetic conductor sidewalls in this example is unphysical, it demonstrates the use of a general-purpose algorithm to examine the material-dependence of the Casimir force. If we wished to use dispersive

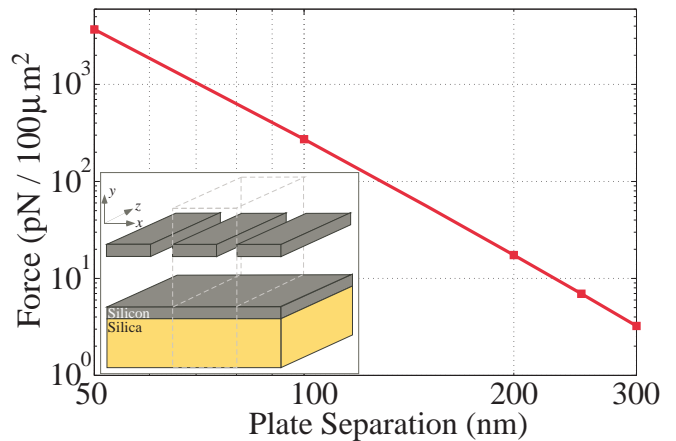


FIG. 8: The Casimir force between a periodic array of Silicon waveguides and a Silicon/Silica substrate, as the array/substrate separation is varied. The system is periodic in the x -direction and translation-invariant in the z -direction, so the computation involves a set of two-dimensional simulations.

and/or anisotropic materials, no additional code would be required.

D. Periodic Boundary Conditions

Periodic dielectric systems are of interest in many applications. The purpose of this section is to demonstrate computations involving a periodic array of dispersive silicon dielectric waveguides above a silica substrate, shown in Fig. 8.

As discussed in Ref. 12, the Casimir force for periodic systems can be computed as an integral over all Bloch wavevectors in the directions of periodicity. Here, as there are two directions, x and z , that are periodic (the latter being the limit in which the period goes to zero). The force is then given by:

$$\int_0^\infty \int_0^\infty F_{k_z, k_x} dk_z dk_x \quad (10)$$

where F_{k_z, k_x} is the force computed from one simulation of the unit cell using Bloch-periodic boundary conditions with wavevector $\mathbf{k} = (k_x, 0, k_z)$. In the present case, the unit cell is of period $1\mu\text{m}$ in the x direction and of zero length in the z direction, so the computations are effectively two-dimensional (although they must be integrated over k_z).

We use the dispersive model of Eq. (7) for silicon, while for silica we use [8]

$$\epsilon(\omega) = 1 + \sum_{j=1}^3 \frac{C_j \omega_j^2}{\omega_j^2 - \omega^2} \quad (11)$$

where $(C_1, C_2, C_3) = (0.829, 0.095, 1.098)$ and $(\omega_1, \omega_2, \omega_3) = (0.867, 1.508, 203.4) \times 10^{14}$ (rad/sec).

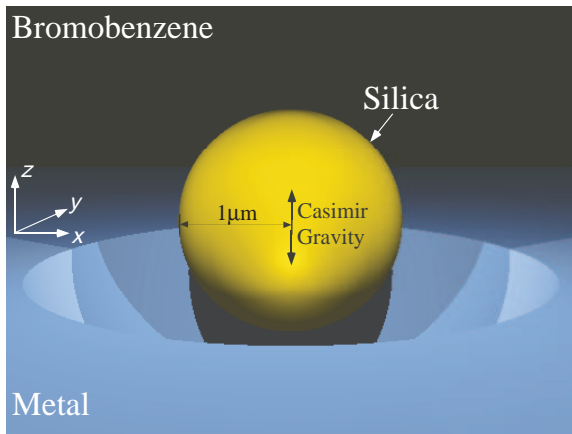


FIG. 9: Three-dimensional configuration showing stable levitation. At the equilibrium point, the force of gravity counters the Casimir force, while the Casimir force from the walls of the spherical indentation confine the sphere laterally

E. Full 3d computations

As a final demonstration, we compute the Casimir force for a fully three-dimensional system, without the use of special symmetries. The system used is depicted in Fig. 9.

This setup demonstrates stable levitation with the aid of a fluid medium, which has been explored previously in Ref. 9. With this example, we present a setup similar to that used previously to measure repulsive Casimir forces [6], with the hope that this system may be experimentally feasible.

A silica sphere sits atop a perfect metal plane which has a spherical indentation in it. The sphere is immersed in bromobenzene. As the system satisfies $\epsilon_{\text{sphere}} < \epsilon_{\text{fluid}} < \epsilon_{\text{plane}}$, the sphere feels a repulsive Casimir force upwards [6]. This is balanced by the downward force of gravity, which confines the sphere vertically. In addition, the Casimir repulsion from the sides of the spherical indentation confine the sphere in the lateral direction. The radius of the sphere is $1\mu\text{m}$, and the circular indentation in the metal is formed from a circle of radius $2\mu\text{m}$, with a center $1\mu\text{m}$ above the plane. For computational simplicity, in this model we neglect dispersion and use the zero-frequency values for the dielectrics, as the basic effect does not depend upon the dispersion (the precise values for the equilibrium separations will be changed with dispersive materials). These are $\epsilon = 2.02$ for silica and $\epsilon = 4.30$.

An efficient strategy to determine the stable point is to first calculate the force on the glass sphere when its axis is aligned with the symmetry axis of the indentation. This configuration is cylindrically-symmetric and can be efficiently computed as in the previous section. Results for a specific configuration, with a sphere radius of 500 nm and an indentation radius of $1\mu\text{m}$, are shown in Fig. 10.

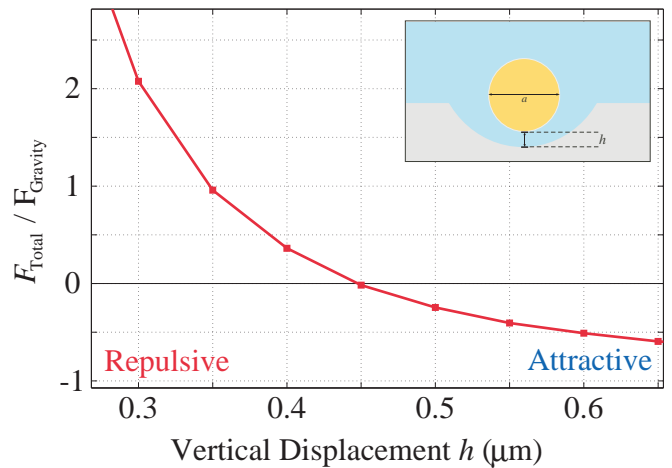


FIG. 10: Total (Casimir + gravity) vertical (z) force on the silica sphere (depicted in the inset) as the height h of the sphere's surface above the indentation surface is varied. The point of vertical equilibrium occurs at $h \sim 450$ nm.

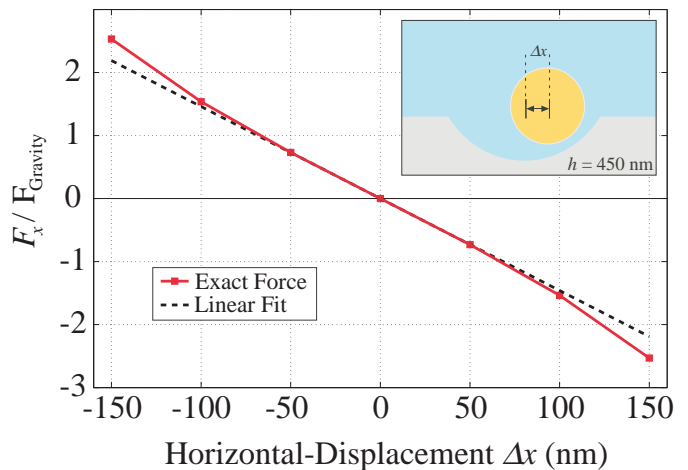


FIG. 11: Casimir restoring force on the sphere as a function of lateral displacement dx , when the vertical position is fixed at $h = 450$ nm, the height at which gravity balances the Casimir force

The force of gravity is balanced against the Casimir force at a height of $h = 450$ nm. To determine the strength of lateral confinement, we perform a fully three-dimensional computation in which the center of the sphere is displaced laterally from equilibrium by a distance dx (the vertical position is held fixed at the equilibrium value $h = 450$ nm). The results are shown in Fig. 11. It is seen that over a fairly wide range ($|\Delta x| < 100$ nm) the linear term is a good approximation to the force, whereas for larger displacements the Casimir force begins to increase more rapidly. Of course, at these larger separations the vertical force is no longer zero, due to the curvature of the indentation, and so must be re-computed as well.

The fully three-dimensional computations are rather

large, and require roughly a hundred CPU hours per force point. However, these Casimir calculations parallelize very easily – every source term, polarization, and k -point can be computed in parallel, and individual FDTD calculations can be parallelized in our existing software – so we can compute each force point in under an hour on a supercomputer (with 1000+ processors). In contrast, the 2d and cylindrical calculations require tens of minutes per force point. We believe that this method is usable in situations involving complex three-dimensional materials (e.g, periodic systems or systems with anisotropic materials).

IV. CONCLUDING REMARKS

We have demonstrated a practical implementation of a general FDTD method for computing Casimir forces via a harmonic expansion in source currents. The utility of such a method is that many different systems (dispersive, anisotropic, periodic boundary conditions) can all be simulated with the same algorithm.

In practice, the harmonic expansion converges rapidly with higher harmonic moments, making the overall computation complexity of the FDTD method $O(N^{1+1/d})$ for N grid points and d spatial dimensions. This arises from the $O(N)$ number of computations needed for one FDTD time step, while the time increment used will vary inversely with the spatial resolution [18], leading to $O(N^{1/d})$ time steps per simulation. In addition, there is a constant factor proportional to the number of terms retained in the harmonic expansion, as an independent simulation is required for each term. For comparison, without a harmonic expansion one would have to run a separate simulation for each point on S . In that case, there would be $O(N^{(d-1)/d})$ points, leading to an overall computational cost of $O(N^2)$ [1].

We do not claim that this is the most efficient technique for computing Casimir forces, as there are other works that have also demonstrated very efficient methods capable of handling arbitrary three-dimensional geometries, such as a recently-developed boundary-element method [13]. However, these integral-equation methods and their implementations must be substantially revised when new types of materials or boundary conditions are desired that change the underlying Green's function (e.g., going from metals to dielectrics, periodic boundary conditions, or isotropic to anisotropic materials), whereas very general FDTD codes, requiring no modifications, are available off-the-shelf.

V. ACKNOWLEDGMENTS

We are grateful to S. Jamal Rahi for sharing his scattering algorithm with us. We are also grateful to Peter Bermel and Ardavan Oskooi for helpful discussions.

VI. APPENDIX

A. Simplified computation of $g(t)$

In Ref. 1 we introduced a geometry-independent function $g(t)$, which resulted from the Fourier transform of a certain function of frequency, termed $g(\xi)$, which is given by [1]:

$$g(\xi) = -i\xi \left(1 + \frac{i\sigma}{\xi}\right) \frac{1 + i\sigma/2\xi}{\sqrt{1 + i\sigma/\xi}} \Theta(\xi) \quad (12)$$

Once $g(t)$ is known, it can be integrated against the fields in time, allowing one to compute a decaying time-series which will, when integrated over time, yield the correct Casimir force.

$g(\xi)$ has the behavior that it diverges in the high-frequency limit. For large ξ , $g(\xi)$ has the form:

$$g(\xi) \rightarrow g_1(\xi) \equiv \frac{\xi}{i} \Theta(\xi) + \sigma \Theta(\xi) \text{ as } \xi \rightarrow \infty \quad (13)$$

Viewing $g_1(\xi)$ as a function, we could only compute its Fourier transform $g_1(t)$ by introducing a cutoff in the frequency integral at the Nyquist frequency, since the time signal is only defined up to a finite sampling rate and the integral of a divergent function may appear to be undefined in the limit of no cutoff.

Applying this procedure to compute $g(-t)$ yields a time series that has strong oscillations at the Nyquist frequency. The amplitude of these oscillations can be quite high, increasing the time needed to obtain convergence and also making any physical interpretation of the time series more difficult.

These oscillations are entirely due to the high-frequency behavior of $g(\xi)$, where $g(\xi) \sim g_1(\xi)$. However, $g(t)$ and $g(\xi)$ only appear when they are being integrated against smooth, rapidly decaying field functions $\Gamma(\mathbf{x}, t)$ or $\Gamma(\mathbf{x}, \xi)$. In this case, g can be viewed as a tempered distribution (such as the δ -function) [30]. Although $g(\xi)$ diverges for large ξ , this divergence is only a power law, so it is a tempered distribution and its Fourier transform is well-defined without any truncation. In particular, the Fourier transform of $g_1(\xi)$ is given by:

$$g_1(-t) = \frac{i}{2\pi} \left(\frac{1}{t^2} + \frac{\sigma}{t} \right) \quad (14)$$

Adding and subtracting the term $g_1(\xi)$ from $g(\xi)$, the remaining term decays to zero for large ξ and can be Fourier transformed numerically without the use of a high-frequency cutoff, allowing $g(-t)$ to be computed as the sum of $g_1(t)$ plus the Fourier transform of a well-behaved function. This results in a much smoother $g(-t)$ which will give the same final force as the $g(-t)$ used in Ref. 1, but will also have a much more well-behaved time dependence.

In Fig. 12 we plot the convergence of the force as a function of time for the same system using the $g(-t)$

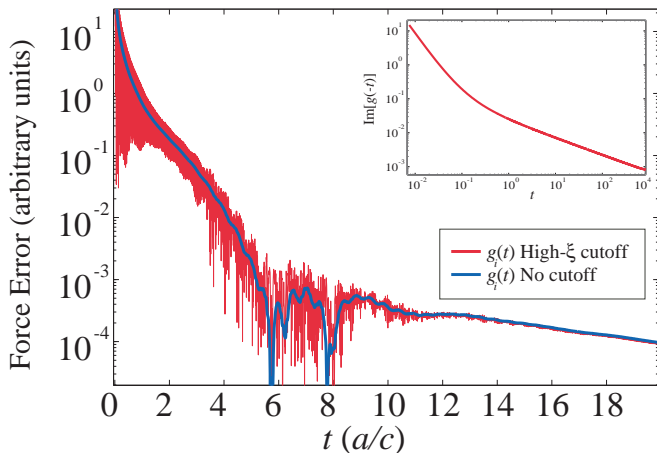


FIG. 12: Plot of the force error (force after a finite time integration vs. the force after a very long run time) for $g(t)$ determined from a numerical transform as in Ref. 1 and from the analytic transform of the high-frequency components. Inset: $\text{Im}[g(-t)]$ obtained without a cutoff, in which the high-frequency divergence is integrated analytically. Compare with Fig. 1 of Ref. 1

obtained by use of a high-frequency cutoff and for one in which $g_1(\xi)$ is transformed analytically and the remainder is transformed without a cutoff. The inset plots $\text{Im}g(-t)$ obtained without using a cutoff (since the real part is not used in this paper) for $\sigma = 10$. If a complex harmonic basis is used, one must take care to use the full $g(t)$ and not only its imaginary part.

1. Further simplification

In addition to the treatment of the high-frequency divergence in the previous section, we find it convenient to also Fourier transform the low-frequency singularity of $g(\xi)$ analytically. As discussed in Ref. 1, the low-frequency limit of $g(\xi)$ is given by:

$$g(\xi) \rightarrow g_2(\xi) \equiv \frac{\sqrt{i} \sigma^{3/2}}{2 \xi^{1/2}} \Theta(\xi) \text{ as } \xi \rightarrow 0 \quad (15)$$

The Fourier transform of $g_2(\xi)$, viewed as a distribution, is:

$$g_2(-t) = \frac{i \sigma^{3/2}}{4\sqrt{\pi} t^{1/2}} \quad (16)$$

After removing both the high- and low-frequency divergences of $g(\xi)$, we perform a numerical Fourier transform on the function $\delta g(\xi) \equiv g(\xi) - g_1(\xi) - g_2(\xi)$, which is well-behaved in both the high- and low-frequency limits.

In the present text we are only concerned with real sources, in which case all fields $\Gamma(\mathbf{x}, t)$ are real and only the imaginary part of $g(-t)$ contributes to the force in Equation (1). The imaginary part of $g(-t)$ is then:

$$\text{Im}[g(-t)] = \text{Im}(\delta g(-t)) + \frac{1}{2\pi} \left(\frac{1}{t^2} + \frac{\sigma}{t} \right) + \frac{1}{4\sqrt{\pi}} \frac{\sigma^{3/2}}{t^{1/2}} \quad (17)$$

2. Perfect conductors and z -invariance

As discussed in Ref. 12, the stress-tensor frequency integral for a three-dimensional z -invariant system involving only vacuum and perfect metallic conductors is identical in value to the integral of the stress tensor for the associated two-dimensional system (corresponding to taking a $z = 0$ cross-section), with an extra factor of $i\omega/2$ in the frequency integrand. In the time domain, this corresponds to solving the two-dimensional system with a new $g(-t)$.

In this case the Fourier transform can be performed analytically. The result is:

$$\text{Im}[g(-t)] = \frac{1}{2\pi} \left(\frac{2}{t^3} + \frac{3\sigma}{2t^2} + \frac{\sigma^2}{2t} \right) \quad (18)$$

B. Harmonic expansion in cylindrical coordinates

The extension of the above derivation to three dimensions and non-Cartesian coordinate systems is straightforward, as the only difference is in the representation of the δ -function. Because the case of rotational invariance presents some simplification, we will explicitly present the result for this case below.

For cylindrical symmetry, we work in cylindrical coordinates (r, ϕ, z) and choose a surface S that is also rotationally invariant about the z -axis. S is then a surface of revolution, consisting of the rotation of a parametrized curve $(r(s), \phi = 0, z(s))$ about the z axis. The most practical harmonic expansion basis consists of functions of the form $f_n(x)e^{im\phi}$. Given a ϕ dependence, many FDTD solvers will solve a modified set of Maxwell's Equations involving only the (r, z) coordinates. In this case, for each m the problem is reduced to a two-dimensional problem where both sources and fields are specified only in the (r, z) -plane.

Once the fields are determined in the (r, z) -plane, the force contribution for each m is given by:

$$\int_0^{2\pi} d\phi \int_S ds_j(\mathbf{x}) r(\mathbf{x}) e^{-im\phi} \int_0^{2\pi} d\phi' \int_S ds(\mathbf{x}') r(\mathbf{x}') e^{im\phi'} \delta_S(\mathbf{x} - \mathbf{x}') \Gamma_{ij;m}^E(t; \mathbf{x}, \mathbf{x}') \quad (19)$$

where the values of \mathbf{x} range over the full three-dimensional (r, ϕ, z) system. Here we introduce the

Cartesian line element ds along the one-dimensional surface S in anticipation of the cancellation of the Jacobian factor $r(\mathbf{x})$ from the integration over S . We have explicitly written only the contribution for Γ^E , the contribution for Γ^H being identical in form.

In cylindrical coordinates, the representation of the δ -function is:

$$\delta(\mathbf{x} - \mathbf{x}') = \frac{1}{2\pi r(\mathbf{x})} \delta(\phi - \phi') \delta(r - r') \delta(z - z') \quad (20)$$

For simplicity, assume that S consists entirely of $z = \text{constant}$ and $r = \text{constant}$ surfaces (the more general case follows by an analogous derivation). In these cases, the surface δ -function δ_S is given by:

$$\begin{aligned} \delta_S(\mathbf{x} - \mathbf{x}') &= \frac{1}{2\pi r(\mathbf{x})} \delta(\phi - \phi') \delta(r - r'), & z = \text{constant} \\ \delta_S(\mathbf{x} - \mathbf{x}') &= \frac{1}{2\pi r(\mathbf{x})} \delta(\phi - \phi') \delta(z - z'), & r = \text{constant} \end{aligned}$$

In either case, we see that upon substitution of either form of δ_S into Eq. (19), we obtain a cancellation with the first $r(\mathbf{x})$ factor. Now, one picks an appropriate decomposition of δ_S into functions f_n (a choice of $r = \text{const}$ or $z = \text{const}$ merely implies that the f_n will either be functions of z , or r , respectively). We denote either case as $f_n(\mathbf{x})$, with the r and z dependence implicit.

We now consider the contribution for each value of n . The integral over \mathbf{x}' is:

$$\Gamma_{ij;nm}^E(t, \mathbf{x}) = \int_0^{2\pi} d\phi' \int_S ds(\mathbf{x}') r(\mathbf{x}') \Gamma_{ij;nm}^E(t, \mathbf{x}, \mathbf{x}') f_n(\mathbf{x}') e^{im\phi'}$$

As noted in the text, $\Gamma_{ij;nm}^E(t, \mathbf{x})$ is simply the field measured in the FDTD simulation due to a three-dimensional current source of the form $f_n(\mathbf{x})e^{im\phi}$. In

the case of cylindrical symmetry, this field must have a ϕ dependence of the form $e^{im\phi}$:

$$\Gamma_{ij;nm}^E(t, r, z, \phi) = \Gamma_{ij;nm}^E(t, r, z) e^{im\phi} \quad (21)$$

This factor of $e^{im\phi}$ cancels with the remaining $e^{-im\phi}$. The integral over ϕ then produces a factor of 2π that cancels the one introduced by δ_S . After removing these factors, the problem is reduced to one of integrating the field responses entirely in the (r, z) plane. The contribution for each n and m is then:

$$\int_S ds_j(\mathbf{x}) \bar{f}_n(\mathbf{x}) \Gamma_{ij;nm}^E(t, r, z) \quad (22)$$

If one chooses the $f_n(\mathbf{x})$ to be real-valued, the contributions for $+m$ and $-m$ are related by complex conjugation. The sum over m can then be rewritten as the real part of a sum over only non negative values of m . The final result for the force from the electric field terms is then:

$$F_i = \int_0^\infty dt \text{Im}[g(-t)] \sum_n \int_S ds_j(r, z) f_n(r, z) \Gamma_{ij;n}^E(t, r, z) \quad (23)$$

where the m -dependence has been absorbed into the definition of $\Gamma_{ij;n}$ as follows:

$$\Gamma_{ij;n}^E(t, r, z) \equiv \Gamma_{ij;n,m=0}^E(t, r, z) + 2 \sum_{m>0} \text{Re}[\Gamma_{ij;nm}^E(t, r, z)] \quad (24)$$

We have also explicitly included the dependence on r and z to emphasize that the integrals are confined to the two-dimensional (r, z) plane. The force receives an analogous contribution from the magnetic-field terms.

-
- [1] A. W. Rodriguez, A. P. McCauley, J. D. Joannopoulos, and S. G. Johnson, *Phys. Rev. A* **80**, 012115 (2009).
[2] H. B. G. Casimir, *Proc. K. Ned. Akad. Wet.* **51**, 793 (1948).
[3] T. H. Boyer, *Phys. Rev. A* **9**, 2078 (1974).
[4] S. K. Lamoreaux, *Phys. Rev. Lett.* **78**, 5 (1997).
[5] H. B. Chan, V. A. Aksyuk, R. N. Kleinman, D. J. Bishop, and F. Capasso, *Science* **291**, 1941 (2001).
[6] J. Munday, F. Capasso, and V. A. Parsegia, *Nature* **457**, 170 (2009).
[7] M. Antezza, L. P. Pitaevskii, S. Stringari, and V. B. Svetovoy, *Phys. Rev. Lett.* **97**, 223203 (2006).
[8] A. Rodriguez, M. Ibanescu, D. Iannuzzi, F. Capasso, J. D. Joannopoulos, and S. G. Johnson, *Phys. Rev. Lett.* **99**, 080401 (2007).
[9] A. W. Rodriguez, J. Munday, D. Davlit, F. Capasso, J. D. Joannopoulos, and S. G. Johnson, *Phys. Rev. Lett.* **101**, 190404 (2008).
[10] T. Emig, N. Graham, R. L. Jaffe, and M. Kardar, *Phys. Rev. Lett.* **99**, 170403 (2007).
[11] T. Emig, *Phys. Rev. Lett.* **98**, 160801 (2007).
[12] A. Rodriguez, M. Ibanescu, D. Iannuzzi, J. D. Joannopoulos, and S. G. Johnson, *Phys. Rev. A* **76**, 032106 (2007).
[13] H. T. M. Reid, A. W. Rodriguez, J. White, and S. G. Johnson, *Phys. Rev. Lett.* **103**, 040401 (2008).
[14] S. Pasquali and A. C. Maggs, *J. Chem. Phys.* **129**, 014703 (2008).
[15] S. Pasquali and A. C. Maggs, *Phys. Rev. A (R)* **79**, 020102 (2009).
[16] H. Gies and K. Klingmuller, *Phys. Rev. Lett.* **97**, 220405 (2006).
[17] F. M. Serry, D. Walliser, and M. G. Jordan, *J. Appl. Phys.* **84**, 2501 (1998).
[18] A. Taflove and S. C. Hagness, *Computational Electrodynamics: The Finite-Difference Time-Domain Method*

- (Artech, Norwood, MA, 2000).
- [19] A. Farjadpour, D. Roundy, A. Rodriguez, M. Ibanescu, P. Bermel, J. Burr, J. D. Joannopoulos, and S. G. Johnson, *Opt. Lett.* **31**, 2972 (2006).
- [20] A. P. McCauley, A. W. Rodriguez, and S. J. Johnson, *Casimir meep wiki*, http://ab-initio.mit.edu/wiki/index.php/Casimir_calculations_in_Meep.
- [21] L. D. Landau, E. M. Lifshitz, and L. P. Pitaevskii, *Statistical Physics Part 2*, vol. 9 (Pergamon Press, Oxford, 1960).
- [22] S. J. Rahi, A. W. Rodriguez, T. Emig, R. L. Jaffe, S. G. Johnson, and M. Kardar, *Phys. Rev. A* **77**, 030101 (2008).
- [23] R. K. Rao and P. Yip, *Discrete Cosine Transform: Algorithms, Advantages, Applications* (Academic Press, Boston, 1990).
- [24] J. P. Boyd, *Chebyshev and Fourier Spectral Methods* (Dover, New York, 2001), 2nd ed.
- [25] M. Li, W. H. P. Pernice, and H. X. Tang, arXiv:atom-ph/0903.5117 (2009).
- [26] M. L. Povinelli, M. Loncar, M. Ibanescu, E. J. Smythe, S. G. Johnson, F. Capasso, and J. D. Joannopoulos, *Opt. Lett.* **30**, 3042 (2005).
- [27] E. M. Lifshitz, *Dokl. Akad. Nauk. SSSR* **100**, 879 (1955).
- [28] I. E. Dzyaloshinskiĭ, E. M. Lifshitz, and L. P. Pitaevskii, *Adv. Phys.* **10**, 165 (1961).
- [29] V. M. Marachevsky, *Phys. Rev. D* **75**, 085019 (2007).
- [30] W. Rudin, *Real and Complex Analysis* (McGraw-Hill, New York, 1966).
- [31] Non-orthogonal functions may be used, but this case greatly complicates the analysis and will not be treated here.